Experimental and Theoretical Study of Raman Scattering in Tl⁺-Doped Alkali Halides*

Richard T. Harley

Physics Department, Northwestern University, Evanston, Illinois 60201

and

John B. Page, Jr.

Physics Department, Arizona State University, Tempe, Arizona 85281

and

Charles T. Walker

Physics Department, Northwestern University, Evanston, Illinois 60201

(Received 4 August 1970)

Experimental Raman spectra are presented for KCl, KBr, KI, and RbCl doped with Tl⁺ ions. The spectra are continuous and first order, being caused by the impurity-induced breakdown of the lattice periodicity, and are strongest for E_g vibrations and weaker for T_{2g} vibrations. No A_{1g} spectra are seen. Theoretical calculations for the Raman spectra are presented and are based on the assumption that the electron-phonon interaction is linear in the displacements of the impurity's nearest neighbors. The spectra are calculated using phonons derived both from the shell model as fit to neutron data for KBr and KCl, and from the breathing-shell model computed from macroscopic parameters for all four hosts. The best agreement between theory and experiment is seen to occur using zero-force-constant changes for the E_g spectra in KBr and KI and for the T_{2g} spectra in all hosts. In KCl, a 10% stiffening in the force constant is necessary for the E_g spectrum, and in RbCl this spectrum requires a 10% weakening. No significant differences can be seen in the spectra calculated from the two different models for the phonons, and the agreement between theory and experiment is good.

I. INTRODUCTION

In this paper, we report an experimental and theoretical study of the first-order impurity-induced Raman spectra of Tl⁺-doped KCl, KBr, KI, and RbCl.

Raman scattering from the vibrational modes of a pure crystal is governed by two universal selection rules. The first, resulting from the periodicity of the lattice, requires that the change in photon momentum equal the change in crystal momentum. This, combined with the relative wavelengths of visible light and the lattice vibrations, restricts first-order Raman activity to phonons with almost zero wave vector. For second- and higher-order processes, the *sum* of the wave vectors of the phonons involved must be almost zero. The second rule is discussed in detail in Sec. III. It states that for crystals containing a center of inversion, the only vibrational modes which are Raman active in first order are those having displacement patterns which are even under inversion, i.e., even-parity modes. The $\vec{k} \approx 0$ and inversion-symmetry rules thus require that for a first-order Raman-active mode in a pure crystal, all atoms located at centers of inversion are at rest.

These two rules lead to severe restrictions in alkali halides. All atoms in crystals of the rocksalt structure are at centers of inversion. Hence, none of the zero-wave-vector phonons is of even parity and there is no first-order Raman spectrum. Instead, one observes a continuous second-order

spectrum.

However, when a substitutional impurity is introduced into an alkali halide, the translational symmetry and the inversion symmetry for all atoms but the impurity are broken; this makes first-order Raman scattering possible. The spectra will be continuous because the loss of translational invariance removes the zero-wave-vector selection rule. But, since the impurity itself occupies a center of inversion, the scattering is still restricted to modes which are even under inversion about the impurity site; that is, to modes in which the impurity does not move. The impurity-induced Raman spectra will reflect the perturbed crystal density of states weighted according to the amplitudes of motion of the neighboring ions for modes of even parity. The spectra will have peaks where these "projected densities of states" have peaks. Any remaining modes in which the impurity ion itself moves will not be Raman active but will be infrared active. These modes are odd under inversion.

The amplitudes and frequencies of these infrared-active modes are dependent on the defect mass as well as the force constants in the perturbed crystal. A given impurity may produce phonon resonances, gap modes, or true localized modes. The Raman-active modes involve no defect motion and are therefore independent of the impurity mass; they are determined solely by the force constants in the perturbed crystal and the masses of the neighbors of the impurity. If the force constants are substantially changed from the pure crystal values, phonon

resonances, gap modes, or localized modes may again be induced so that the vibrational spectra would bear little relation to those for the pure crystal. However, if the force constants in the perturbed crystal are the same as in the pure crystal, the Raman-active vibrational modes will be identical with the equivalent modes in the pure crystal, the Raman effect would then serve as a direct probe of the vibrational spectrum for the pure crystal. Impurities such as these are known as isotopic. It is important to bear in mind that they are isotopic in the lattice-dynamical sense, but not in terms of the electron-phonon interaction. Indeed, the fact that the electron-phonon interaction with impurities present differs from that for the pure host is what gives rise to the impurity-induced Raman effect.

Although the study of phonon resonances, gap modes, and localized modes is of interest in itself, in order to get information about the pure-crystal phonons it is desirable to study the spectra for isotopic defects.

In an earlier report,[1] we display our results for KBr doped with low concentrations of Tl^+, and it was seen that one observed a first-order Raman spectrum. In that paper, we also display a comparison of our room-temperature data on $KBr:Tl^+$ with a theoretical Raman spectrum computed using phonons derived from the breathing-shell model (BSM), using zero-force-constant changes. The comparison, in that case, was very good indeed, and suggested that Tl^+ acted as an isotopic impurity in KBr allowing one to use the Raman effect as a probe of the pure-crystal phonons. In that paper, we also gave a few tabulated experimental and theoretical results for $KCl:Tl^+$ and $KI:Tl^+$.

There has been a considerable amount of previous experimental and theoretical work on impurity-induced Raman spectra (see, for example, Ref. 2). Perhaps the most complete studies have been made on crystals containing F centers. Raman scattering from F centers in KCl and NaCl was observed by Worlock and Porto,[3] and discussed theoretically by Kleinman,[4] Benedek and Nardelli,[5] and Henry and Slichter.[6] A combined experimental and theoretical investigation of F centers in KF, NaBr, and RbF was made by Buchenauer, Fitchen, and Page.[7] While one can see effects of the lattice phonons in these studies, they are complicated by the large force-constant perturbations produced by the F center. Further, the experiments were done with a resonance enhancement arising from the coincidence between the exciting laser frequency and the absorption band for the F center, resulting in some subtle complications in the spectra. The same remarks pertain to the Raman spectra due to $F_A(Li)$ centers in KCl observed by Fritz.[8]

Raman scattering from localized modes has been observed by Feldman, Ashkin, and Parker[9] for Ge

in Si, and by Harrington, Harley, and Walker[10] for H^- and D^- in CaF_2, SrF_2, and BaF_2. However, localized modes are not involved in the present problem. Stekhanov and co-workers[11] have looked at KCl doped with Li, Br, I, Na, Rb, and Cs. They interpreted their spectra as indicating scattering by phonon resonances and localized vibrations. Some near-resonance features of their data were discussed by Rebane and Tehver,[12] but there are some ambiguities in their results; in particular, Kaiser and Möckel[13] have been unable to reproduce the KCl:Li and KCl:I data.

Kaiser and Möller[14] have observed first-order impurity-induced scattering in NaCl:Ag, but the system is known to be one for which the impurity force constants differ from the host crystals.[15] Lastly, Hurrel et al.[16] have observed a first-order scattering in KBr containing 8% KCl, but at this concentration, as they pointed out, one may have a highly disordered lattice and the interpretation would not be straightforward.

Therefore, it appears that Tl^+ in KCl, KBr, KI, and RbCl is the first clear-cut example of an impurity to be studied by Raman scattering for which the force-constant changes are very small.[1,17,18]

A theory of impurity-induced first-order Raman scattering in alkali-halide crystals has been developed by Xinh, Maradudin, and Coldwell-Horsfall (XMC).[19] They calculated spectra for the particular case of KCl and did their numerical evaluation using $0\,°K$ deformation-dipole-model (DDM) phonons. More accurate theoretical phonons now exist and are used in this paper. In addition, our calculations have been made with a finer wave vector and frequency mesh than was used by XMC. This makes a far more detailed comparison between experiment and theory possible.

The reminder of this paper is arranged as follows: In Sec. II, the experimental details and results are displayed. The data were taken at $15\,°K$ since at these low temperatures anharmonic effects and also the host-crystal second-order Raman spectra can be ignored. Section III is a review of the theory, while Sec. IV describes the calculations made with $0\,°K$ BSM- and shell-model (SM) phonons assuming both zero and small force-constant changes. The theoretical curves which, in our opinion, fit the data best are displayed for direct comparison with experiment, whereas the results for different force-constant changes for the two models are given in Appendix B. In Sec. V, we give further discussion, and the article is summarized in Sec. VI.

II. EXPERIMENT

A. Experimental Details

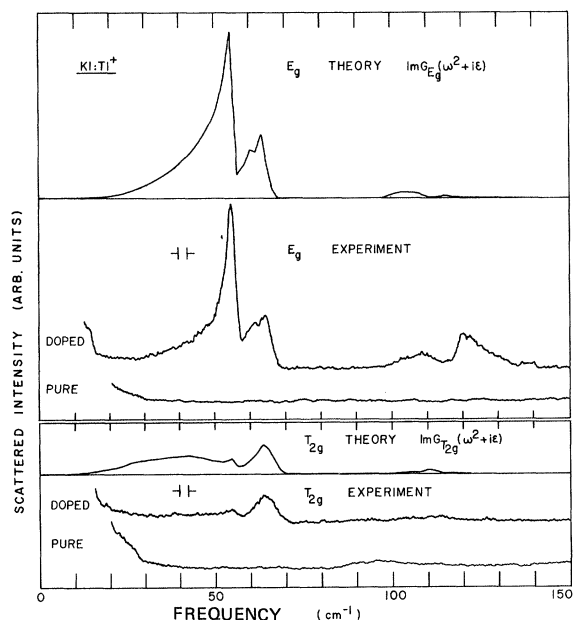The samples used in this work came from several sources. Pure crystals and also our sample of

FIG. 1. Experimental and theoretical Raman spectra for KI : Tl$^+$: above E_g component, below T_{2g} component. The temperature of the experiments was 15 °K and the instrumental gain was the same for both doped and pure crystals and for E_g and T_{2g} spectra. The theoretical curves are for zero force-constant change and were computed using 0 °K BSM phonons. They have been normalized to reflect the experimental intensities.

KI:Tl$^+$ were obtained from Harshaw Chemical Co. Samples of KCl:Tl$^+$, KBr:Tl$^+$, and RbCl:Tl$^+$ were grown at Northwestern University by the Kyropoulos method, and our most concentrated sample of KCl:Tl$^+$ was grown by the Bridgeman method at Cornell University and kindly supplied to us by Professor Pohl. For KCl:Tl$^+$ and KBr:Tl$^+$, we studied crystals of several different concentrations and found that the impurity-induced Raman spectra scaled with concentration. Only one concentration each of KI:Tl$^+$ and RbCl: Tl$^+$ was studied. The data presented here are for our most concentrated samples which contained 8.6×10^{19}, $\approx 1 \times 10^{19}$, 6×10^{18}, and $\approx 1 \times 10^{19}$ cm^{-3} for KCl:Tl$^+$, KBr:Tl$^+$,KI: Tl$^+$, and RbCl:Tl$^+$, respectively. At these concentrations it should be a good approximation to regard the impurities as isolated since the average distance between them is at least 50 Å.

The spectra were recorded using a Coherent-Radiation model 52 argon-ion laser operating with 1.3 W in the 488.0-nm line and a Spex double monochromator with photon-counting detection. The usual 90° scattering geometry was used. In order to improve the signal to noise and to work with as high a resolution as possible, the spectra were repeatedly swept and the signal accumulated in a multichannel memory unit (Enhancetron 1024 or

Fabritek 4074). The samples were cooled to 15 °K using liquid helium in an optical cryostat of conventional design.

Although the absolute accuracy of the spectra recorded with this equipment was ± 2 cm^{-1} due to possible spectrometer errors, the relative positions of peaks within one spectrum were accurate to less than 1 cm^{-1}.

The point group for these materials is O_h. As will be seen in Sec. III, the first-order impurity-induced spectra are composed of components resulting from vibrations belonging to the A_{1g}, E_g, and T_{2g} irreducible representations. The symmetry properties of the observed spectra were determined using various combinations of propagation direction of incident light $\vec{k}$, polarization of incident light $\vec{\epsilon}$, and the selected polarization of scattered light (propagating perpendicular to $\vec{k}$) $\vec{\epsilon}'$, relative to the crystal axes. With $\vec{k} \parallel \langle 001 \rangle$, $\vec{\epsilon} \parallel \langle 110 \rangle$, and $\vec{\epsilon}' \parallel \langle 001 \rangle$, the spectra of T_{2g} character were observed; E_g components were selected with $\vec{k} \parallel \langle 001 \rangle$, $\vec{\epsilon} \parallel \langle 110 \rangle$, and $\vec{\epsilon}' \parallel \langle 1\bar{1}0 \rangle$, while combined E_g and A_{1g} spectra were recorded with $\vec{k} \parallel \langle 001 \rangle$, $\vec{\epsilon} \parallel \langle 010 \rangle$, and $\vec{\epsilon}' \parallel \langle 010 \rangle$. In these arrangements, the weights of the three symmetries are[20] T_{2g}, $3E_g$, and $A_{1g} + 4E_g$.

B. Experimental Results

The experimental E_g and T_{2g} Stokes spectra for all four Tl$^+$-doped samples are shown in Figs. 1–5. The spectra were recorded at 15 °K using the same instrumental gain and resolution for the two symmetries in a given sample. Also shown are the results of theoretical calculations which are discussed in Sec. III. The experimental spectra for undoped samples, taken at equivalent sensitivity to the doped spectra, are shown for reference in the cases of KBr, KI, and RbCl. The pure-crystal spectra for KCl are not shown, but at this temperature and sensitivity they are essentially zero between 0 and 200 cm^{-1}.

All the Tl$^+$-doped crystals show strong lines of E_g symmetry and rather weaker T_{2g} spectra. A particularly striking feature is the similarity of the spectra for KI:Tl$^+$ (Fig. 1) and KBr:Tl$^+$ (Fig. 2). Both crystals have a very prominent E_g peak which cuts off sharply on the high-energy side; the remaining smaller E_g peaks and the T_{2g} spectra are also very similar in form for the two crystals. However, the peaks in KBr:Tl$^+$ occur at higher energies than those in KI:Tl$^+$. KCl:Tl$^+$ (Figs. 3 and 4) shows the most intense T_{2g} spectrum of the four samples, the intensity being comparable to that of the E_g spectrum. Note that the Tl$^+$-induced lines in KCl occur at considerably higher energy than in KI or KBr. RbCl:Tl$^+$ (Fig. 5) shows a very sharp E_g line which has a width of approximately 2.7 cm^{-1}. (The width of the peak in Fig. 5 is limited by the instrumental resolution.) There are also two

broader and weaker bands in the E_g spectrum of
RbCl:Tl[+] at 58 and 89 cm^{-1}. RbCl:Tl[+] shows the
weakest T_{2g} spectrum of the four samples.

We were not able to detect any impurity-induced
lines of A_{1g} symmetry. However, the level of de-
tection for A_{1g} was not as high as for E_g and T_{2g}
modes because it is not possible to observe A_{1g}
spectra independently of E_g or T_{2g}. In addition the
pure crystals generally show a more intense sec-
ond-order scattering of A_{1g} symmetry than of E_g
or T_{2g} symmetry. A direct evaluation of the A_{1g}
scattering strength can be seen by comparing Figs.
3 and 6. Figure 3 shows only the E_g spectrum for
KCl:Tl[+], while Fig. 6 shows the combined E_g and
A_{1g} spectra, both taken at 15°K. Even though the
vertical scales are not the same in the two figures,
it is clear that any A_{1g} scattering is 10% or less of
the E_g strength. Any A_{1g} spectra are comparably
weak in KBr, KI, and RbCl. It should be noted that
the reason for the very low intensity of the pure-
crystal second-order scattering is that at these
frequencies the spectra are composed mainly of
difference bands, for which the Raman-scattering
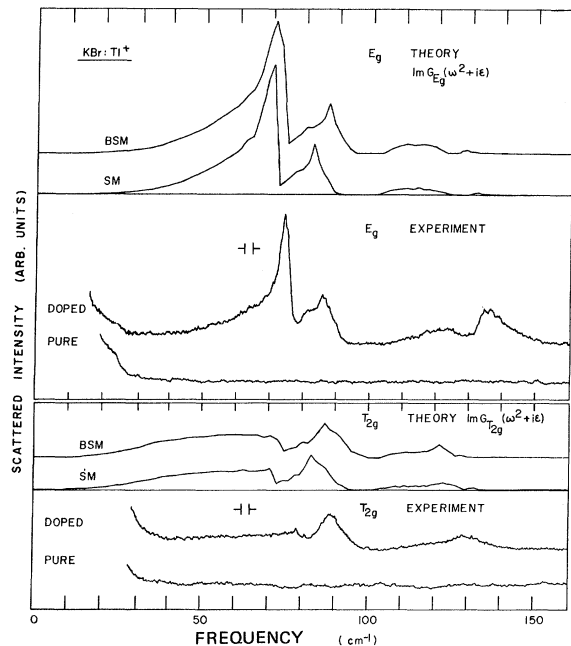efficiency vanishes as the temperature approaches
zero.

FIG. 3. Experimental and theoretical Raman spectra
of KCl:Tl[+]: E_g component. The temperature of the ex-
periment was 15°K and the instrumental gain was the same
as that of the T_{2g} component shown in Fig. 4. The theo-
retical curves are for a 10% increase in the longitudinal
force constants between the Tl[+] and its nearest neighbors,
and the calculations were made using 0°K BSM and 115°K
SM (VI) phonons. The theoretical spectra have been
normalized to reflect the experimental intensity.

FIG. 2. Experimental and theoretical Raman spectra
for KBr:Tl[+]: above E_g component, below T_{2g} component.
The temperature of the experiment was 15°K and the in-
strumental gain was the same for both doped and pure
crystals and for E_g and T_{2g} spectra. The theoretical
curves are for zero force-constant change and were com-
puted using 0°K BSM and 90°K SM (VI) phonons. They
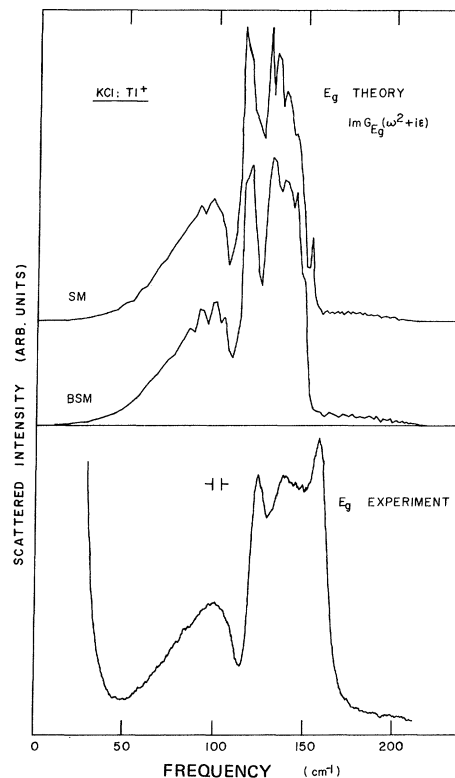have been normalized to reflect the experimental intensi-
ties.

Although it is not the purpose of this article to
discuss temperature-dependent effects, for conve-
nience we list in Table I the experimental peak
positions for E_g and T_{2g} spectra of all four hosts.
A discussion of phonon renormalization effects will
be published separately.

The evidence that our impurity-induced spectra
are first order is twofold. First, we have observed
that the intensities of the lines in the Stokes spectra
have a temperature dependence appropriate to first-
order scattering. One cannot use the temperature
dependence of the ratio of Stokes to anti-Stokes in-
tensities to determine the order of the scattering,
since for a given value of the Raman shift the tem-
perature dependence of this ratio is the same for
all orders. However, first-order scattering can
be distinguished from second order by observing
the over-all temperature dependence of either the
Stokes or the anti-Stokes intensity.

The second piece of evidence that the defect-induced
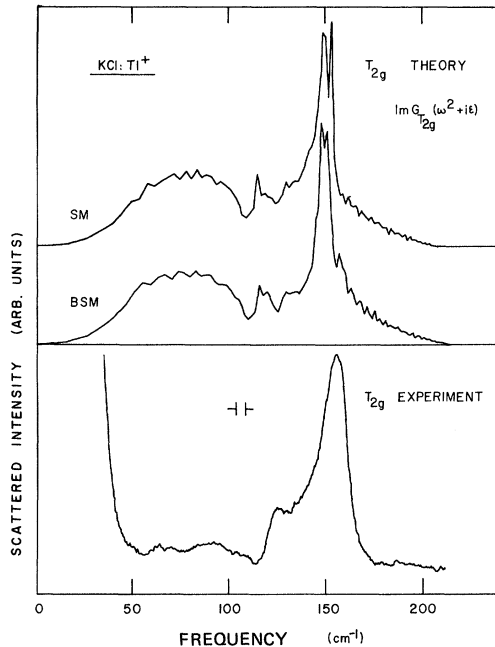spectra are first order is that such intense scat-

KCl: Tl⁺ ... SM ... BSM ... T₂g THEORY ... ImG_{T₂g} (ω²+iε)

⊣ ⊢ ... T₂g EXPERIMENT

SCATTERED INTENSITY (ARB. UNITS)

FREQUENCY (cm⁻¹)

FIG. 4. Experimental and theoretical Raman spectra of KCl : Tl⁺: T_{2g} component. The temperature of the experiment was 15 °K and the instrumental gain was the same as for the E_g component shown in Fig. 3. The theoretical curves are for zero force-constant changes and were computed using 0 °K BSM and 115 °K SM (VI) phonons. They have been normalized to reflect the experimental intensities.

roughly equal scattering at frequencies in the optic- and acoustic-phonon regions.

The experimental spectra show these effects. For KI:Tl⁺ and KBr:Tl⁺, strong peaks appear at frequencies corresponding to acoustic phonons of the pure crystals, and there are energy gaps in which no Raman scattering occurs that correspond well with the gaps between the acoustic- and optic-phonon regions in the host lattices.[21,22] At higher energies, there is a pair of much weaker lines corresponding to optic phonons. RbCl also has a gap between the acoustic and optic branches,[23] but the intense E_g line and the T_{2g} band in the RbCl:Tl⁺ spectra correspond to optic-phonon frequencies, while the very weak low-energy E_g lines correspond to acoustic modes. The KCl:Tl⁺ spectra, as expected, show scattering which covers the whole range of acoustic- and optic-phonon frequencies[24,25] with almost equal intensity.

The success of this qualitative interpretation is strong evidence that a good quantitative description of the impurity-induced spectra can be made by as-

tering is produced by very small concentrations of impurities (less the 0.5 mole%); it seems unlikely that in alkali halides such a small disturbance of the lattice could induce second-order scattering of comparable or greater intensity than that from the pure crystal.

If the force constants are assumed to be only weakly perturbed, the defect-induced spectra can be explained in a qualitative way by considering the relative masses of the cations and anions in the crystals. If one assumes that the Raman process takes place via a virtual excited electronic state of the Tl⁺ ion, and that only the motions of the nearest neighbors appreciably modulate the Tl⁺ electronic wave functions, then the defect-induced Raman spectra should be most intense in regions of the phonon spectrum where the nearest neighbors of the Tl⁺ vibrate with large amplitudes; more precisely, where the projected density of states is large. This will be at frequencies in the acoustic-phonon region if the nearest neighbors, which are the anions, happen to be the heavier ions in the crystal, as is the case in KI or KBr, and will be in the optic-phonon region if the anions are lighter than the cations, as in RbCl. If the anions and cations are of comparable mass, as in KCl, one would expect

TABLE I. Experimental peak positions for Tl⁺-induced spectra at three temperatures. Values for sharp lines are accurate to ±2 cm⁻¹. All entries in cm⁻¹.

Crystal and symmetry		Peak position		
		300 °K	80 °K	15 °K
RbCl	E_g	45	58	58
		85	90	89
		103	113	113
	T_{2g}	130	140	140
KCl	E_g	90	100	100
		120	125	125
		134	140	140
		149	159	159
	T_{2g}	120	125	125
		148	157	157
KBr	E_g	70	74	74
		84	86	86
		117	121	122
		129	135	135
	T_{2g}	(70)	(74)	78
		82	86	89
		...	127	130
KI	E_g	51	55	55
		60	63	65
		99	103	108
		113	115	120
	T_{2g}	(50)	(54)	(54)
		62	64	64
		...	...	112

suming weak force-constant perturbations and considering the influence on the Tl^+ of just its nearest neighbors. These ideas will be made more precise in Sec. III.

III. THEORY

The calculations reported here are based upon the off-resonance theory of Maradudin[26] and Benedek and Nardelli[5] for an insulator obeying the Born-Oppenheimer approximation. In order to keep the present work complete and self-contained and to illuminate some of the important points, a rather thorough outline of the theory will now follow.

Under the assumption that the incident-photon energies are small compared with any of those for electronic transitions in the perturbed crystal, Maradudin,[26] following Born and Huang,[27] showed that the intensity of linearly polarized Raman scattering per unit solid angle per unit frequency is given by

$$I(\omega_s) = \frac{\omega_i^4}{2\pi c^3} \sum_{\alpha\beta\gamma\lambda} n_\alpha n_\beta i_{\alpha\gamma,\beta\lambda}(\omega) \underline{E}_\gamma(\omega_i) \underline{E}_\lambda^*(\omega_i). \quad (1)$$
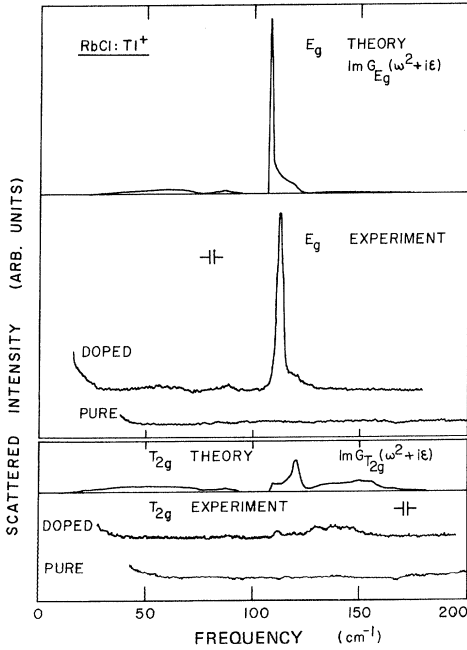

FIG. 5. Experimental and theoretical Raman spectra of RbCl:Tl⁺: above E_g component, below T_{2g} component. The temperature of the experiment was 15 °K and the instrumental gain was the same for both pure and doped crystals and for E_g and T_{2g} components. The theoretical curves were computed using 0 °K BSM phonons. The theoretical E_g spectrum is for a 10% decrease in the longitudinal force constants between the defect and its nearest neighbors, while the T_{2g} spectrum is for unperturbed force constants. The theoretical curves have been normalized to reflect the experimental intensities.
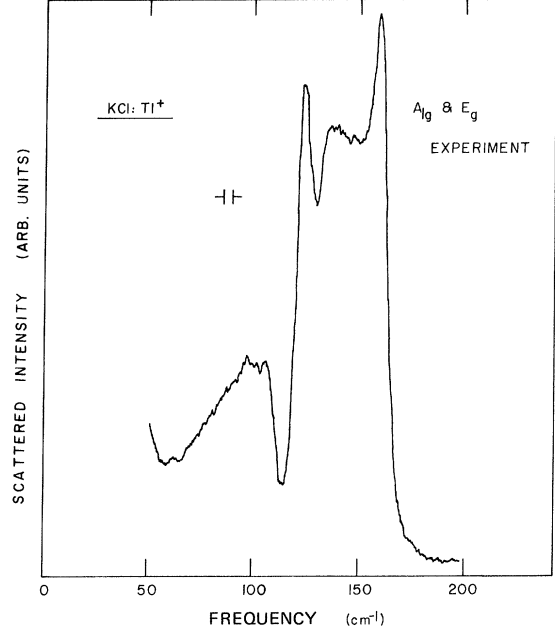

FIG. 6. Experimental Raman spectrum for KCl:Tl⁺: combined A_{1g} and E_g components taken at 15 °K with different instrumental gain from that of Figs. 3 and 4.

Here $\omega = \omega_s - \omega_i$ is the frequency difference between the scattered and incident radiation, $\hat{n}$ is a unit vector parallel to the scattered electric field, and $\underline{E}(\omega_i)$ is the Fourier component of the incident electric field. The Raman-scattering tensor $i_{\alpha\gamma,\beta\lambda}(\omega)$ is given by

$$i_{\alpha\gamma,\beta\lambda}(\omega) = (2\pi)^{-1} \int_{-\infty}^{\infty} d\tau \, e^{-i\omega\tau} \langle \mathcal{P}_{\alpha\gamma}^*(\underline{u}, \tau) \mathcal{P}_{\beta\lambda}(\underline{u}) \rangle, \quad (2)$$

where $\mathcal{P}_{\beta\lambda}(\underline{u})$ is the operator for the static electronic polarizability of the crystal in a fixed nuclear configuration $\underline{u}$ and in its ground electronic state; the brackets denote a thermal average over nuclear configurations, and

$$\mathcal{P}_{\alpha\gamma}(\underline{u}, \tau) = e^{iH\tau/\hbar} \mathcal{P}_{\alpha\gamma}(\underline{u}) e^{-iH\tau/\hbar}$$

is $\mathcal{P}_{\alpha\gamma}(\underline{u})$ in the interaction representation. In terms of the system's electronic states $|\mu\rangle$ for nuclear configuration $\underline{u}$ and its dipole moment operator

$$\mathfrak{M} = \sum_n q_n \underline{u}_n + \sum_e q_e \underline{u}_e,$$

where q_n and q_e denote the nuclear and electronic charges; the static polarizability tensor operator is given explicitly by

$$\mathcal{P}_{\alpha\gamma}(\underline{u}) = \sum_{\mu\neq0} (\hbar\omega_{\mu0})^{-1} (\langle 0|\mathfrak{M}_\alpha|\mu\rangle \langle\mu|\mathfrak{M}_\gamma|0\rangle + c.c.), \quad (3)$$

with $\omega_{\mu0}$ being the frequency for a virtual transition to state $|\mu\rangle$. According to this equation, $\mathcal{P}_{\alpha\gamma}(\underline{u})$ is both real and symmetric.

In the harmonic approximation, the Hamiltonian for the perturbed crystal can be written

$$H = \tfrac{1}{2}(\underline{\dot{u}}^T \underline{M}\,\underline{\dot{u}} + \underline{u}^T \underline{\Phi}\,\underline{u}) = \tfrac{1}{2}\sum_f (\dot{d}_f^2 + \omega_f^2 d_f^2), \qquad (4)$$

where the normal coordinates d_f and nuclear displacements from equilibrium $\underline{u} = \{u(n\alpha)\}$ are related through

$$\underline{u} = \sum_f \underline{\chi}(f)\,d_f. \qquad (5)$$

The symbols $\underline{M}$ and $\underline{\Phi}$ denote the system's mass and harmonic force-constant matrices, and the coefficients $\underline{\chi}(f)$ are the normalized eigenvectors satisfying

$$(\underline{\Phi} - \omega_f^2 \underline{M})\,\underline{\chi}(f) = 0 \quad \text{and} \quad \underline{\chi}^T(f)\,\underline{M}\,\underline{\chi}(f') = \delta_{ff'}. \qquad (6)$$

Expanding the polarizability tensor in terms of the normal coordinates gives

$$\mathcal{P}_{\alpha\gamma}(\underline{u}) = P_{\alpha\gamma,0} + \sum_f P_{\alpha\gamma,f}\,d_f + \cdots , \qquad (7)$$

so that

$$\langle \mathcal{P}_{\alpha\gamma}(\underline{u}, \tau)\,\mathcal{P}_{\beta\gamma}(\underline{u})\rangle$$

$$= P_{\alpha\gamma,0}P_{\beta\lambda,0} + \sum_{ff'} P_{\alpha\gamma,f}P_{\beta\lambda,f'}\,\langle d_f(\tau)\,d_{f'}\rangle + \cdots , \qquad (8)$$

where use has been made of the harmonic result $\langle d_f(\tau)\rangle = 0$. When substituted into (2), the constant term above just contributes $\delta(\omega)$, corresponding to Rayleigh scattering, and will not be considered further. If the $\langle d_f(\tau)\,d_{f'}\rangle$ term is worked out in the harmonic approximation and substituted into (2), the result is first-order Raman scattering, given by

$$i_{\alpha\gamma,\beta\lambda}(\omega) = \hbar \sum_f (2\omega_f)^{-1} P_{\alpha\gamma,f} P_{\beta\lambda,f}\,[\eta(\omega_f)\,\delta(\omega + \omega_f)$$
$$+ \eta(-\omega_f)\,\delta(\omega - \omega_f)], \qquad (9)$$

where

$$\eta(\omega) = (1 - e^{-\beta\hbar\omega})^{-1}$$

and the two terms give the Stokes and anti-Stokes contributions, corresponding to phonon emission and absorption, respectively. Just the Stokes component will be subsequently considered, as only they persist at low temperatures.

Symmetry arguments may be used to determine which modes lead to vanishing coefficients $P_{\alpha\beta,f}$ and are thus Raman inactive. The polarizability tensor is first expanded in terms of particles displacements according to

$$\mathcal{P}_{\alpha\beta}(\underline{u}) = P_{\alpha\beta,0} + \sum_{m\gamma} P_{\alpha\beta}(m\gamma)\,u(m\gamma) + \cdots , \qquad (10)$$

with $m = 1, \ldots, Ns$, there being s atoms in the basis and N unit cells, while $\gamma = x, y, z$. This equation, together with Eq. (5), leads to the relation

$$P_{\alpha\beta,f} = \sum_{m\gamma} P_{\alpha\beta}(m\gamma)\,\chi(m\gamma \mid f) \qquad (11)$$

connecting the first-order coefficients in the normal coordinate and particle displacement representations. Now because $\mathcal{P}_{\alpha\beta}(\underline{u})$ relates two vectors, namely, the electric field and its associated polarization, this quantity transforms under point-symmetry operations as a second-rank Cartesian tensor. Then, since $P_{\alpha\beta}(m\gamma)$ is just the first derivative of $\mathcal{P}_{\alpha\beta}(\underline{u})$ with respect to $u(m\gamma)$ evaluated at the system's equilibrium configuration, it follows that $P_{\alpha\beta}(m\gamma)$ is a third-rank tensor. Thus, if $\underline{r}$ is the 3×3 orthogonal Cartesian matrix of a point-symmetry operation taking the particle at site m to site m', then

$$P_{\alpha\beta}(m\gamma) = \sum_{\alpha'\beta'\gamma'} r_{\alpha'\alpha} r_{\beta'\beta} r_{\gamma'\gamma} P_{\alpha'\beta'}(m'\gamma'). \qquad (12)$$

If the system has inversion symmetry about site $m = 0$ and the sites are labeled so that site m is transformed under inversion to site $-m$, one immediately has

$$P_{\alpha\beta}(m\gamma) = -P_{\alpha\beta}(-m\gamma). \qquad (13)$$

In particular, $P_{\alpha\beta}(0\gamma) = 0$. Hence, if *every* site is an inversion center, as is the case in pure crystals of the NaCl structure, all $P_{\alpha\beta}(m\gamma)$ vanish and first-order Raman scattering is not allowed. The introduction of a single defect at $m = 0$ into such a crystal, however, removes all of the inversion centers except at the defect itself, so that first-order Raman scattering is possible. The remainder of this discussion will be restricted to this situation, namely, a single-substitutional defect in a rocksalt lattice. The point group is thus O_h, the full cubic group.

Now the $\underline{\chi}(f)$'s are $3Ns$-dimensional basis vectors for irreducible representations of the point group and are thus either even or odd under inversion in the defect site, that is,

$$\chi(-m\gamma \mid f) = \pm \chi(m\gamma \mid f)$$

for f referring to an even (-) or odd (+) parity mode. This fact, together with Eqs. (11) and (13), immediately yields the result that only even-parity modes can give rise to first-order Raman scattering.

For the cubic group there are five irreducible representations corresponding to even-parity modes, but group theory further reduces the number of first-order Raman-active modes to three. This is because the $\underline{r}$ matrices are just the matrices of the irreducible representation $T_{1u}(\Gamma_{15})$ according to which Cartesian vectors transform, so that Eq. (12) states that $P_{\alpha\beta}(m\gamma)$ is the $(m\gamma)$ component of a $3Ns$-dimensional basis vector $\underline{P}_{\alpha\beta}$ belonging to the $\alpha\beta$ row of the direct-product representation $T_{1u} \times T_{1u}$. Hence, in view of Eq. (11) and the orthogonality of basis vectors belonging to different irreducible representations, $P_{\alpha\beta,f}$ can be nonzero only when $\underline{\chi}(f)$ is a basis vector belonging to an irreducible representation contained in $T_{1u} \times T_{1u}$. This restricts f to modes of $A_{1g}(\Gamma_1)$, $E_g(\Gamma_{12})$, $T_{1g}(\Gamma_{15'})$, and $T_{2g}(\Gamma_{25'})$

symmetry. Finally, by using group-theoretic projection operators to project symmetry vectors of these four types from $\underline{P}_{\alpha\beta}$ for different values of $\alpha\beta$, one finds that the only possible nonzero $P_{\alpha\beta,f}$ are $P_{\alpha\alpha,A_{1g}}$, $P_{\alpha\alpha,E_g}$, and $P_{\alpha\beta,T_{2g}}$, where $\alpha \neq \beta$. The T_{1g} projection dropped out when use was made of the fact that $\mathcal{P}_{\alpha\beta}(\underline{u})$ is a symmetric tensor.

The Raman-scattering tensor $i_{\alpha\gamma,\beta\lambda}$, being proportional to the product of two second-rank tensors, is a fourth ranked Cartesian tensor. This plus the fact that $P_{\alpha\beta}(\underline{u})$ is real and symmetric, results in there being but three independent elements of $i_{\alpha\gamma,\beta\lambda}$ for cubic crystals, [26] namely,

$$i_{xx,xx} \equiv i_{11}, \quad i_{xx,yy} \equiv i_{12}, \quad \text{and} \quad i_{xy,xy} \equiv i_{44}.$$

Returning to Eq. (11), rewriting it as $P_{\alpha\beta,f} = \underline{P}_{\alpha\beta}^T \times \underline{\chi}(f)$, and substituting this into the Stokes term of Eq. (9) gives

$$i_{\alpha\gamma,\beta\lambda}(-\omega) = \hbar\eta(\omega)\, \underline{P}_{\alpha\gamma}^T \sum_f \underline{\chi}(f)\, \underline{\chi}^T(f)\, \delta(\omega_f^2 - \omega^2)\, \underline{P}_{\beta\lambda},$$
(14)

where ω is now the absolute value $|\omega_s - \omega_i|$ of the frequency shift of the scattered radiation. This equation is conveniently rewritten in terms of the system's harmonic Green's-function matrix

$$\underline{G}(\omega^2) = (\underline{\Phi} - \omega^2\underline{M})^{-1} = \sum_f \underline{\chi}(f)\, \underline{\chi}^T(f)\delta(\omega_f^2 - \omega^2)^{-1} \quad (15)$$

as

$$i_{\alpha\gamma,\beta\lambda}(-\omega) = \pi^{-1}\hbar\eta(\omega)\, \text{Im}\, \underline{P}_{\alpha\gamma}^T\, \underline{G}(z)\, \underline{P}_{\beta\lambda}, \quad (16)$$

with $z = \omega^2 + i\epsilon$ and the limit $\epsilon \to 0^+$ being understood. In the following, we will often omit showing the explicit z dependence of $\underline{G}$. If the Green's-function matrix is now expanded in terms of a complete orthonormal set $\{\xi(\Gamma_i t)\}$ of basis vectors for the irreducible representations of O_h according to

$$\underline{G} = \sum_{itt'} G_B(\Gamma_i tt')\, \underline{\xi}(\Gamma_i t)\, \underline{\xi}^T(\Gamma_i t'),$$

where Γ_i denotes a representation, t labels the vectors within a representation, and the matrix elements of $\underline{G}$ in the symmetry basis are given by
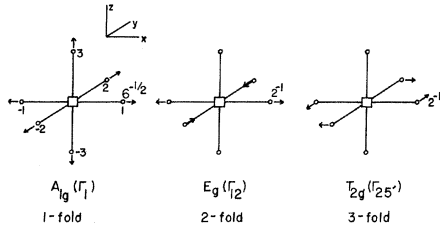

FIG. 7. Normalized symmetry basis vectors on the defect's nearest neighbors for the first-order Raman-active modes. Degeneracies are indicated, and only one partner of each symmetry is shown. The particle labeling convention is given in the A_{1g} figure.

$$G_B(\Gamma_i tt') = \underline{\xi}^T(\Gamma_i t)\, \underline{G}\, \underline{\xi}(\Gamma_i t'), \quad (17)$$

one has

$$i_{\alpha\gamma,\beta\lambda}(-\omega) = \pi^{-1}\hbar\eta(\omega)\, \text{Im} \sum_{itt'} G_B(\Gamma_i tt')$$

$$\times \underline{P}_{\alpha\gamma}^T \underline{\xi}(\Gamma_i t)\, \underline{P}_{\beta\lambda}^T \underline{\xi}(\Gamma_i t'). \quad (18)$$

In view of the symmetry arguments given earlier, the sum over i may be restricted to include just the irreducible representations A_{1g}, E_g, and T_{2g}.

It has been seen that the introduction of a defect at $m = 0$ allows, in principle, all of the $P_{\alpha\beta}(m\gamma)$ coefficients to be nonzero, except at the site $m = 0$ itself, which retains inversion symmetry. We will now assume that the only $P_{\alpha\beta}(m\gamma)$ coefficients having values appreciably different from zero are those for which m refers to one of the defect's six nearest neighbors. Physically, we are just supposing that the dominant first-order electron-phonon coupling is through the motion of the impurity's nearest neighbors. Hence, in both Eqs. (17) and (18) just the nearest-neighbor components of the symmetry basis vectors need to be considered, and these are shown for A_{1g}, E_g, and T_{2g} modes in Fig. 7.

Knowledge of these vectors allows one to work out the scalar products $\underline{P}_{\alpha\gamma}^T \underline{\xi}(\Gamma_i t)$. The result for A_{1g} modes is

$$\underline{P}_{xx}^T \underline{\xi}(A_{1g}) = 2 \cdot 6^{-1/2}\left[P_{xx}(1x) + 2P_{xx}(2y)\right],$$

where the initial factor of 2 arises from the application of Eq. (13), and use has been made of the fact that $P_{xx}(3z)$ is equal to $P_{xx}(2y)$, which follows from Eq. (12), applied for a rotation of $90°$ about the x axis. Clearly, $\underline{P}_{yy}^T \underline{\xi}(A_{1g})$ is equal to $\underline{P}_{xx}^T \underline{\xi}(A_{1g})$, so that one may write

$$\underline{P}_{xx}^T \underline{\xi}(A_{1g}) = \underline{P}_{yy}^T \underline{\xi}(A_{1g}) = 2 \cdot 6^{-1/2}(A + 2C), \quad (19a)$$

with A and C being $P_{xx}(1x)$ and $P_{xx}(2y)$, respectively. Proceeding similarly for the twofold degenerate E_g modes, one obtains

$$\underline{P}_{xx}^T \underline{\xi}(E_g 1) = -\underline{P}_{yy}^T \underline{\xi}(E_g 1) = A - C$$
and
(19b)
$$\underline{P}_{xx}^T \underline{\xi}(E_g 2) = \underline{P}_{yy}^T \underline{\xi}(E_g 2) = 3^{-1}\sqrt{3}\,(C - A),$$

whereas the T_{2g} modes give

$$\underline{P}_{xy}^T \underline{\xi}(T_{2g}t) = 2B\,\delta_{t1} \quad (t = 1, 2, 3). \quad (19c)$$

Here B stands for $P_{xy}(1y)$.

It remains now to evaluate the matrix elements of $\underline{G}$ in the symmetry basis according to Eq. (17). Doing so and using the transformation rule

$$G(m\alpha, n\beta) = \sum_{\alpha'\beta'} r_{\alpha'\alpha}\, r_{\beta'\beta}\, G(m'\alpha', n'\beta')$$

satisfied by the Green's-function matrix yields[28]

$$g_B(A_{1g}) = G(1x, 1x) - G(1x, -1x) + 4G(1x, 2y), \quad (20a)$$

$$g_B(E_g\,tt') = \delta_{tt'}[G(1x,\,1x) - G(1x,\,-1x) - 2G(1x,\,2y)],$$

$$\text{(20b)}$$

and

$$g_B(T_{2g}\,tt') = \delta_{tt'}[G(1x,\,1x) - G(1y,\,-1y) + 2G(1x,\,2y)],$$

$$\text{(20c)}$$

where the lower-case g's on the left-hand side of this equation are used to denote that we are working with the nearest-neighbor subspace. The tt' indices will henceforth be dropped because of the $\delta_{tt'}$ factors, which occur because of the vanishing of matrix elements taken with respect to basis vectors belonging to different rows of an irreducible representation. Combining Eqs. (19) and (20) with Eq. (18), one then has for the first-order Stokes scattering

$$i_{11}(-\omega) = \tfrac{2}{3}\pi^{-1}\,\hbar\eta(\omega)\,[(A+2C)^2\,\mathrm{Im}g_B(A_{1g})$$

$$+\,2(A-C)^2\,\mathrm{Im}g_B(E_g)],\qquad\text{(21a)}$$

$$i_{12}(-\omega) = \tfrac{2}{3}\pi^{-1}\,\hbar\eta(\omega)\,[(A+2C)^2\,\mathrm{Im}g_B(A_{1g})$$

$$-\,(A-C)^2\,\mathrm{Im}g_B(E_g)],\qquad\text{(21b)}$$

and

$$i_{44}(-\omega) = 4\pi^{-1}\,\hbar\eta(\omega)\,B^2\,\mathrm{Im}g_B(T_{2g}).\qquad\text{(21c)}$$

Notice that the combinations $i_{11}+2i_{12}$, $i_{11}-i_{12}$, and i_{44} are proportional to scattering from phonons of the individual symmetry types A_{1g}, E_g, and T_{2g}, respectively. This fact, together with Eq. (1), justifies the experimental arrangements given in Sec. IIA for determining the symmetry properties of the measured spectra.

Now, in general, the presence of defects requires that the Green's functions appearing in Eqs. (21) should be evaluated using perturbed phonons. Since the modes under consideration involve no motion of the defect, they are independent of the impurity mass and are thus perturbed by just the force-constant changes. As will be seen shortly, the force-constant perturbations associated with Tl^+ in KI, KBr, KCl, and RbCl are very weak, and excellent agreement with experiment is available in most cases by using unperturbed phonons. These are plane waves, for which a traveling wave representation with complex χ's is convenient:

$$\chi(lb\alpha\,|\,\vec{k}j) = N^{-1/2}\,e(b\alpha\,|\,\vec{k}j)\,e^{-i\vec{k}\cdot\vec{R}(lb)}.$$

The site index has been split into a cell label $l = 1, \dots, N$ and a basis index $b = b_1, \dots, b_s$. In this work, b_1 and b_2 will refer to positive and negative ions, respectively. The polarization vectors $e(\vec{k}j)$ are eigenvectors of the dynamical matrix

$$D(b\alpha,\,b'\alpha'\,|\,\vec{k}j) = \sum_{l'} \Phi(lb\alpha,\,l'b'\alpha')\,e^{i\vec{k}\cdot\vec{R}(lb,\,l'b')},$$

and they satisfy the orthonormality condition

$$\sum_{b\alpha} m_b e^*(b\alpha\,|\,\vec{k}j)\,e(b\alpha\,|\,\vec{k}j') = \delta_{jj'}\,.$$

The vector $\vec{R}(lb,\,l'b') \equiv \vec{R}(lb) - \vec{R}(l'b')$ connects the equilibrium positions lb and $l'b'$, and with complex polarization vectors the transpose operation appearing in Eq. (15) for the Green's function should be replaced by Hermitian conjugation. Thus, with unperturbed phonons a typical element is given by

$$\mathrm{Im}G_0(1x,\,1x;\,\omega^2) = \pi N^{-1}\sum_{\vec{k}j}\,|e(b_2x\,|\,\vec{k}j)|^2$$

$$\times\,\delta[\omega^2(\vec{k}j) - \omega^2],\qquad\text{(22)}$$

the zero subscript signifying that this is an unperturbed Green's-function element. By averaging Eq. (22) over the interval $(\omega^2,\,\omega^2+\Delta\omega^2)$ one obtains

$$\mathrm{Im}\overline{G}_0(1x,\,1x;\,\omega^2) = \pi(N\Delta\omega^2)^{-1}\sum_{\vec{k}j}\,|e(b_2x\,|\,\vec{k}j)|^2,$$

$$\text{(23)}$$

where the sum is restricted to those $\vec{k}j$'s for which $\omega^2(\vec{k}j)$ is in the interval. By means of this equation and its analogs for the other elements, it is a straightforward task to compute numerical approximations to the unperturbed Green's functions, provided the host-lattice polarization vectors and eigenfrequencies are available. The unperturbed Green's functions are also necessary if the phonons are perturbed by the presence of defects, and the treatment for this case is reviewed in Appendix A.
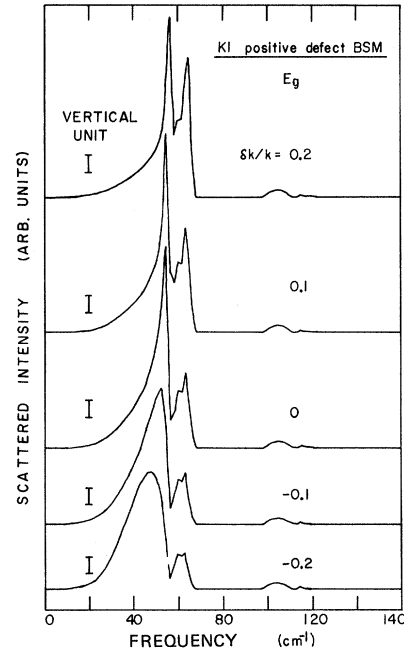

FIG. 8. Perturbed theoretical E_g spectra for KI using 0 °K BSM phonons. The relative vertical scales are indicated by vertical unit bars, and the unperturbed values of the nearest-neighbor longitudinal-overlap force constants are given in Ref. 37.

IV. NUMERICAL CALCULATIONS AND DISCUSSION

We have calculated theoretical Raman spectra according to the theory of Sec. III for a positive impurity in KI, KBr, KCl, and RbCl for the case of unperturbed or weakly perturbed phonons. The force-constant perturbations were assumed to consist of the changes δk_l in the longitudinal force constants between the defect and its six nearest neighbors. This perturbation affects the A_{1g} and E_g modes, whereas the T_{2g} phonons, which involve just "transverse" motion of the defect's nearest neighbors, are independent of δk_l. Of course, the T_{2g} modes will be perturbed by changes δk_t in the transverse nearest-neighbor force constants, but according to the arguments given in Appendix A these changes and the associated perturbations of the T_{2g} Raman spectra should be much weaker than those for for the $A1_g$ and E_g spectra. Thus all of the T_{2g} calculations given here are for unperturbed phonons. The unlikeliness of there being significant force-constant changes beyond those mentioned here is also argued in Appendix A.

The host-lattice phonon frequencies and polarization vectors were obtained for all four hosts from the BSM of Schröder[29] and, for purposes of comparison with the BSM, from the SM of Cowley et al.[22] for KBr and KCl. The SM parameters are determined by fitting to inelastic neutron scattering measurements of the phonon dispersion curves, and the parameter values we have used are given together with the experimental and theoretical dispersion curves for KBr at 90 °K and KCl at 115 °K in Refs. 22 and 24, respectively. The BSM, on the other hand, has few enough parameters that they are obtainable from macroscopic data such as the elastic constants, the high-frequency and static-dielectric constants, the reststrahl frequency, etc., and the data that we have used for KI, KBr, and KCl are given in Table II of Ref. 30. BSM input data for RbCl are also listed in Ref. 30, but these were measured at room temperature. Since the Raman spectra with which we are comparing our calculations were taken at 15 °K, we have used recently measured low-temperature data for RbCl and these are given in Table II. The unperturbed frequencies and core[34] polarization vectors were evaluated for 1686 $\vec{k}$ vectors in the Kellermann $\frac{1}{48}$ sec-

tion of the Brillouin zone. Through symmetry operations, this is equivalent to a uniform mesh of 64 000 $\vec{k}$ vectors.

Numerical approximations to the imaginary parts of the unperturbed host-lattice Green's functions were obtained by dividing the interval $(0, \omega_m^2)$ into 100 bins of equal width $\Delta\omega^2$ and averaging according to Eq. (23) and its analogs for the other required Green's-function elements.[35] The average value for each bin was associated with the bin's frequency midpoint, and the resulting points were connected by straight line segments, yielding the unperturbed imaginary parts given here. The corresponding unperturbed parts, which according to Appendix A are necessary for calculating the perturbed spectra, were computed from Eq. (A4) analytically, this being possible in view of the approximation of the unperturbed imaginary parts as series of straight line segments.

The calculated 0 °K spectra which give the best agreement with experiment are compared with the 15 °K Raman data for E_g and T_{2g} scattering in KI, KBr, KCl, and RbCl in Figs. 1–5. The electron-phonon coupling parameters A, B, and C have been left open, and the vertical scales of the theory curves were therefore chosen to give peak intensities comparable with those of the experimental data. Thus, the ratios of the theoretical E_g and T_{2g} curves reflect the corresponding experimental ratios. The T_{2g} calculations are for unperturbed phonons in all four hosts, whereas in KCl and RbCl the theoretical E_g spectra are for fractional force-constant changes of + 0.1 and – 0.1, respectively.[36] Theoretical E_g spectra for other values of the force-constant changes are given in Appendix B for comparison. Our choice of the best theoretical curves was determined by considering the over-all agreement, taking into account peak positions, relative peak heights, line shapes, and the experimental and theoretical resolutions. As can be seen in the perturbed spectra of Appendix B, the line shapes and relative peak intensities are much more sensitive to force-constant changes than are peak positions.

A. KI : Tl⁺

The best agreement is for KI: Tl⁺ using unperturbed 0 °K BSM phonons as shown in Fig. 1. Indeed,

TABLE II. BSM input parameters for low-temperature phonons in RbCl.

m_1 (amu)	m_2	r_0[a] (cm)	c_{11}[b]	c_{12}[b] (dyne/cm)	c_{44}[b]	ϵ_0[c]	ϵ_∞[c]	ω_0[c] (cm^{-1})	α_1[d] (Å^3)	α_2[d]
85.47	35.45	3.29 $\times 10^{-8}$	4.297 $\times 10^{11}$	0.649 $\times 10^{11}$	0.493 $\times 10^{11}$	4.53	2.20	126.0	1.797	2.974

[a]Computed from the density measurement of Ref. 31.
[b]Measured at 4.2 °K by J. T. Lewis et al., Ref. 31.
[c]Determined for 2 °K by R. P. Lowndes and D. H. Martin, Ref. 32.
[d]Room-temperature data from J. R. Tessman et al., Ref. 33.

for the E_g spectra if account is taken of the experi-
mental resolution of 2.7 cm^{-1} and of the theoretical
bin width of ≈ 2 cm^{-1} at the 55-cm^{-1} peak, the agree-
ment is perfect over the entire acoustic region of
the spectrum. The weaker optical portion is not
well represented by the theory, and this feature of
very good agreement in the acoustic portion accom-
panied by an inadequate comparison in the optical
region also occurs in the E_g results for KBr and
KCl. But note that in KI and KBr, where the near-
est neighbors of the Tl$^+$ are the heavy ions of the
lattice, the major peaks in the nearest-neighbor
projected densities of states occur in the acoustic
region, so that the over-all comparison between
theory and experiment is excellent. The calculated
unperturbed T_{2g} spectrum for KI is also seen to give
excellent agreement with the experimental T_{2g} scat-
tering, which is rather weak.

B. KBr:Tl$^+$

Turning now to Fig. 2 and the KBr:Tl$^+$ spectra,
for which calculations involving both 0 °K BSM and
90 °K SM phonons have been made, we again see
that unperturbed phonons give good agreement with
experiment. As with KI, the E_g agreement is good
in the acoustic region where the experimental res-
olution is 2.7 cm^{-1} and the bin width at the 71-cm^{-1}
peak for the theory curves is ≈ 2 cm^{-1}, whereas the
agreement is poor in the weaker optical portion.
The SM more successfully predicts the lower gap
edge observed in the experimental spectra; how-
ever, the experimental peaks seen near 87 cm^{-1} for
each symmetry are best reproduced by the BSM.

Notice that the BSM and SM E_g and T_{2g} curves are
in good agreement with each other over their entire
frequency range, the principal differences being the
position of the low-frequency edge of the gap be-
tween the acoustic- and optical-phonon branches and
the frequency of the peaks occurring near 85 cm^{-1}
for both symmetries. The predicted positions of
these peaks for the BSM and SM are 87 and 83 cm^{-1},
respectively, and they correspond exactly with
peaks in the frequency densities of states for the
two models. This 5% difference in the positions of
these peaks in the KBr BSM and SM densities of
states is not paralleled by a discrepancy in the KI
BSM and SM[21] densities of states, where the analo-
gous peaks differ only by 2.4% and there is a negli-
gible difference in the position of the gap edge. In
view of this and the strong qualitative similarity be-
tween the KBr and KI results, we have not per-
formed KI SM calculations, which require the addi-
tion of second-neighbor forces between cations to the
the KBr SM. The possibility of attributing the
small differences in the BKr BSM and SM calcula-
tions to the fact that they are appropriate to 0 and
90 °K, respectively, seems to be ruled out by the
fact that according to Table I, the experimental

Raman peaks show no appreciable shift with tem-
perature below 80 °K.

The over-all agreement between theory and ex-
periment is seen to be about equally good for each
model. In addition to the 87-cm^{-1}-peak discrepan-
cies discussed above, both the BSM and SM predict
the main E_g peak to be 3.5 cm^{-1} too low and insuffi-
ciently narrow. This suggests that the E_g phonons
might be perturbed by a slightly increased k_1, but
the perturbed phonon calculations, given in Appen-
dix B, are seen to leave essentially unaltered or to
worsen the relative peak-height and line-shape
agreement without adequately increasing the peak
frequencies.

In summary, then, the best agreement between
theory and experiment for KBr:Tl$^+$ is obtained with
unperturbed phonons. In view of the experimental
and theoretical resolutions, the agreement is good,
and there is no compelling reason to prefer one lat-
tice-dynamical model over the other.

C. KCl:Tl$^+$

Our results for E_g and T_{2g} scattering in KCl:Tl$^+$
are displayed in Figs. 3 and 4. The principal
Raman scattering for this host lattice, whose posi-
tive and negative ions are of nearly equal mass, is
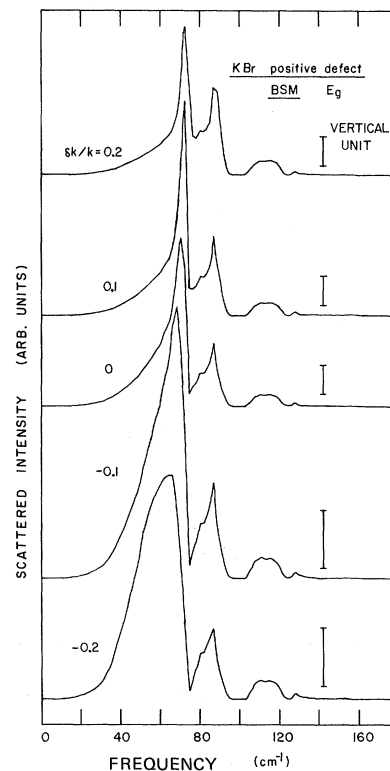seen to occur in both the acoustic and optical

FIG. 9. Same as Fig. 8, but for KBr using 0 °K BSM
phonons.

regions. By comparing the experimental E_g data with the theoretical predictions for unperturbed phonons given in Appendix B, it is apparent that while there is over-all similarity, particularly for the broad acoustic peak near 100 cm^{-1}, the line-shape and peak-height agreements are poor. Allowing the E_g phonons to be perturbed by a 10% increase in k_l results in the substantially improved comparison with experiment exhibited in Fig. 3, where it is seen that the acoustic peak at 100 cm^{-1} in the E_g spectra is well represented by the theory, whereas the theoretical peaks at 116 and 131 cm^{-1} are 9 cm^{-1} short of the experimental peaks at 125 and 140 cm^{-1}, outside the combined experimental resolution of 4.6 cm^{-1} and the theoretical bin width at the 116-cm^{-1} peak of ≈ 2 cm^{-1}. However, a more serious discrepancy occurs for the strong experimental line in the optical region at 159 cm^{-1}, which is not reproduced in either the BSM or SM calculations. There is a weak spike at 154 cm^{-1} in the SM results, but as can be seen from the perturbed phonon calculations given in Appendix B, greater force-constant increases do not sufficiently increase the frequency or strength of this peak and, moreover, worsen the over-all agreement from that given here. We recall that the high-frequency optical-phonon E_g spectra for Tl^{+}-doped KBr and KI were also inadequately described by the theory, but the discrepancy is, of course, more serious in KCl: Tl^{+}, where this region of the spectrum is seen to be dominant.

Kravitz[18] measured the Tl^{+}-induced Raman scattering in KCl at room temperature, and on the basis of comparisons with the calculations of Xinh et al.[19] he also concluded that the force constants are slightly changed. The XMC calculations, as discussed in Sec. I, were done with many fewer $\vec{k}$ vectors and a coarser frequency mesh, using DDM phonons. Thus their calculated spectra have neither the accuracy nor the detail shown here. In addition, the comparison of 0°K theory with room-temperature data, even when the theory is corrected for the Bose-Einstein population factor, is inexact since anharmonic effects are not taken into account (cf. Table I).

The 0°K BSM and 115°K SM results for KCl: Tl^{+} in both the E_g and T_{2g} symmetries are seen to agree with one another to the same extent that they do for KBr: Tl^{+}. The high degree of similarity that we have shown to exist between the corresponding BSM and SM calculations is interesting since the calculations involve the host-lattice polarization vectors as well as frequencies, and furthermore require knowledge of the quantities for $\vec{k}$ vectors throughout the entire Brillouin zone. As stated earlier, the BSM and SM both give good agreement with inelastic neutron scattering measurements of the phonon frequencies. However, these frequencies are usually

measured just for $\vec{k}$ vectors along high-symmetry directions in the Brilloiun zone, and our results show that both the frequencies and polarization vectors of the BSM and SM are essentially the same throughout the zone, at least insofar as these quantities are involved in the $\vec{k}j$ sums in the Green's functions. This agreement between the models is gratifying since the BSM, unlike the SM, is not fit to neutron data and may thus be applied to crystals for which these data are unavailable.

The T_{2g} spectrum for KCl: Tl^{+} is given in Fig. 4, and we see that the agreement between experiment and the calculations for unperturbed phonons is generally good. However, the theory does not reproduce exactly the width of the main peak at 157 cm^{-1}, and the broad theoretical peak at 75 cm^{-1} is of greater intensity than seen experimentally.[37] Nevertheless, the agreement, both over-all and especially for the 157-cm^{-1} peak, is good.

Thus, it appears that Tl^{+} in KCl is accompanied by slightly stiffened longitudinal force constants between the defect and its nearest neighbors, bringing
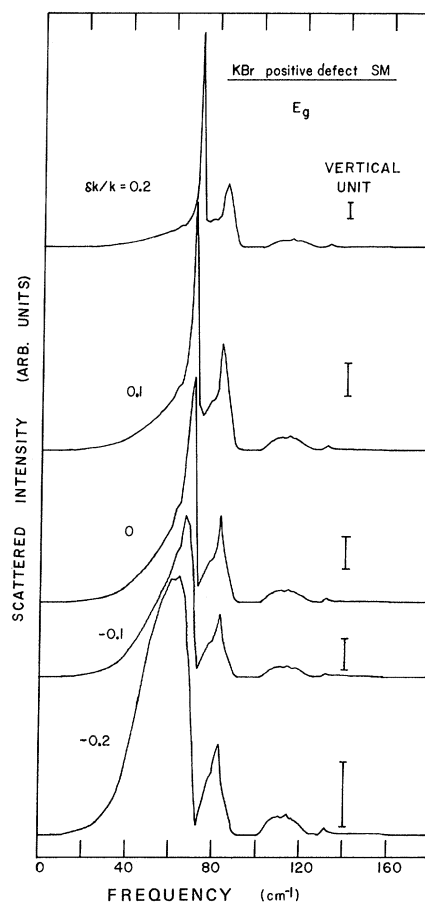

FIG. 10. Same as Fig. 8, but for KBr using 90°K SM (VI) phonons.

the theoretical and experimental E_g spectra into fair agreement except for the 159-cm^{-1} peak. The good T_{2g} agreement leads to the conclusion that these modes are unperturbed by the presence of the impurity.

D. RbCl:Tl$^+$

Finally, the experimental and theoretical E_g and T_{2g} results for RbCl:Tl$^+$ are shown in Fig. 5. The calculations employ BSM phonons derived from the low-temperature input data of Table II, and just as with KCl:Tl$^+$, the experimental E_g spectrum is not well predicted by the unperturbed phonon calculations given in Appendix B. Instead, the best agreement is obtained for the E_g scattering by employing a decrease in k_1 of 10%, in which case the theoretical peak at 108 cm^{-1} is a near resonance associated with the approximate vanishing of the first term in the denominator of the E_g version of Eq. (A5). The theoretical peak is 5 cm^{-1} below the experimental value, but again one must bear in mind the experimental resolution of 2.5 cm^{-1} and the bin width of ≈ 1.5 cm^{-1} at the main peak. Doing so, and noting that the theory reproduces the rather characteristic shoulder on the high-frequency side of the main line and also correctly predicts the relative peak intensities between this peak and the weak acoustic peaks, one sees that the agreement between theory and experiment for the E_g spectrum is good.

The comparison between theory and the very weak experimental T_{2g} spectrum is inadequate. The broad experimental peak near 140 cm^{-1} seems to correspond with the broad theoretical peak near 150 cm^{-1} and the small experimental bump near 115 cm^{-1} may correspond to the theoretical peak at 121 cm^{-1}, but the relative intensities are not reproduced. Unfortunately, the experimental T_{2g} scattering is so weak that a meaningful comparison is difficult to make, and we therefore do not view the T_{2g} discrepancies as serious at this time.

V. FURTHER DISCUSSION AND CONCLUSIONS

The principal discrepancies in the calculated Raman spectra involve the optical portions of the E_g component for KI, KBr, and, more seriously, KCl. This part of the experimental E_g scattering is rather weak for KI and KBr, but is dominant for KCl, and we have seen that the agreement cannot be improved by allowing the E_g phonons to be more strongly perturbed than in Figs. 1–3. We must thus look outside the present theoretical framework. The most obvious possibility suggesting itself is that the unperturbed phonons may be less certain in the optical region of the spectrum than in the acoustic. The flat nature of the dispersion curves for the optical branches results in the peaks in the frequency densities of states being sensitive

to errors in this region. However, the neutron data and their SM interpretations do not appear to be sufficiently uncertain in the optical region, at least in the high-symmetry directions, to allow such an explanation to completely remove the discrepancies. Notice that our projected densities of states for KI and KBr do, in fact, show small peaks at approximately the frequencies corresponding to the observed E_g optical peaks in these crystals, but their strengths are much too weak and their relative intensities are incorrect. For KCl, as mentioned, the SM calculation shows a weak spike at 154 cm^{-1} which does not show in our BSM calculations and which is associated with a peak at 154 cm^{-1} in the KCl SM frequency density of states. This peak has been attributed by Copley et al.[24] to a saddle point occurring at an off-symmetry position in the sixth phonon branch. Unfortunately, the particle amplitudes associated with this peak do not have sufficient E_g projections on to the defect's nearest neighbors to result in a strong 154-cm^{-1} peak in the nearest-neighbor E_g projected density of states.
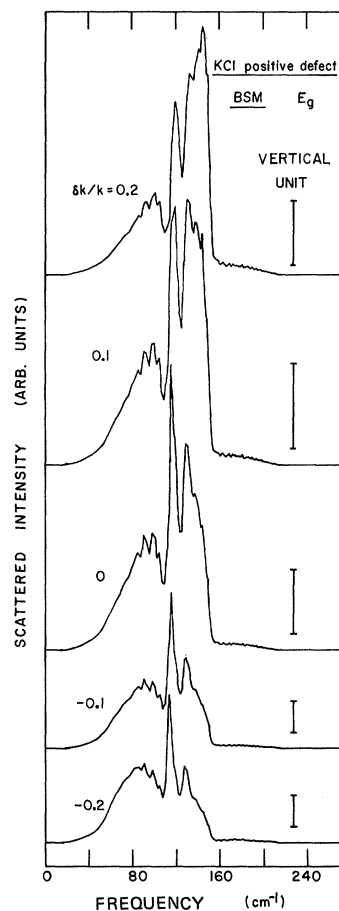

FIG. 11. Same as Fig. 8, but for KCl using 0 °K BSM phonons.

These considerations bring us to another possibility, namely, that the first-order electron-phonon coupling parameters may be appreciable on more than just nearest neighbors of the defect.

If, for instance, the $P_{\alpha\beta}(m\gamma)$'s were assumed to be nonzero on the impurity's second nearest as well as nearest neighbors, the projected densities of states needed in the theory would involve the particle amplitudes for both sets of ions. The defect's second neighbors in KI and KBr are the light potassium ions and should, thus, have large amplitudes in the optical region in contrast to the behavior of the heavy halogen ions which vibrate vigorously in the acoustic portion of the spectrum. The introduction of nonzero second neighbor $P_{\alpha\beta}(m\gamma)$'s would introduce new coupling parameters into the theory, and one would thus be required to attempt an *a priori* estimate of the relative strengths of the nearest- and next-nearest-neighbor contributions in order to complete the theory. This point deserves further study.

In this paper we have not considered questions relating to the Tl$^+$ impurity's electronic properties such as the relative magnitudes of the electron-phonon coefficients A, B, and C which in turn determine the relative strengths of the A_{1g}, E_g, and T_{2g} scattering, the possibility of dynamical Jahn-Teller interactions, nor the electronic origin of the small force-constant changes. To understand these properties theoretically would require detailed knowledge of the Tl$^+$ wave functions, both for the ground and excited states, in each of the hosts. On the other hand, to relate these properties phenomenologically, such as through stress effects on the electronic absorption bands, would require knowledge of the excited states involved in the Raman scattering, and these have not been experimentally determined. The reader interested in the electronic properties associated with Tl$^+$-doped alkali halides should consult the papers of Bimberg et al.,[38] Fowler,[39] Fussgänger,[40] and the references therein.

We have, instead, concentrated on the lattice-dynamical aspects of the problem in order to emphasize the highly successful application of impurity-induced Raman scattering to the study of unperturbed phonons. Introduction of a suitably chosen impurity causes a breakdown of the selection rules which normally forbid first-order Raman scattering in alkali halides. Thus, one is able to probe the entire Brillouin zone with the precision appropriate to optical experiments. The important consideration is that the impurity must cause little or no perturbation of the pure-crystal force constants. This condition is seen to be easily met for the case of Tl$^+$ in the four alkali halides we have studied. In most of the cases we examined, the best agreement between theory and experiment occurred for unper-

turbed phonons; in any case, the most substantial force-constant change we needed was ±10%.

When one considers that there must certainly be other impurities which would produce the same lack of force-constant changes as Tl$^+$, the power of the technique becomes clear. By appropriate choice of impurity one could choose which symmetry phonons he wished to study. By studying these systems under the influence of external perturbations, such as temperature or pressure, one could also study such phenomena as anharmonic interactions. The use of this technique as a probe of unperturbed phonons will clearly be of considerable use in the future.

VI. SUMMARY

In this paper we have studied experimentally and theoretically the Raman spectra produced when Tl$^+$ ions are introduced as impurities in KCl, KBr, KI, and RbCl. The following points were observed:

(i) First-order Raman spectra were observed experimentally, caused by the breakdown of the periodicity of the lattice produced by the Tl$^+$ impurity.
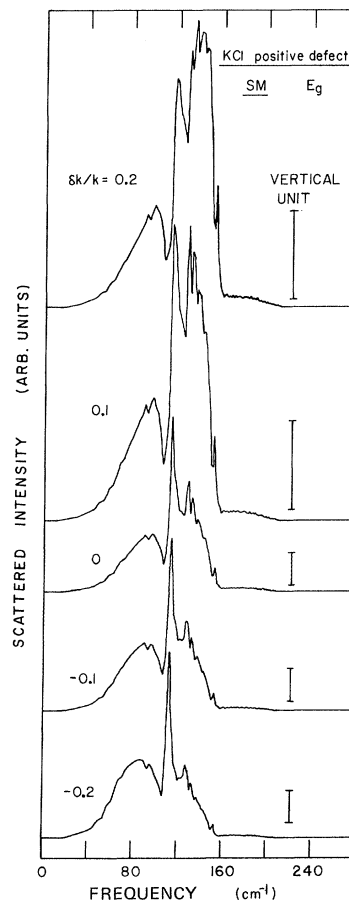
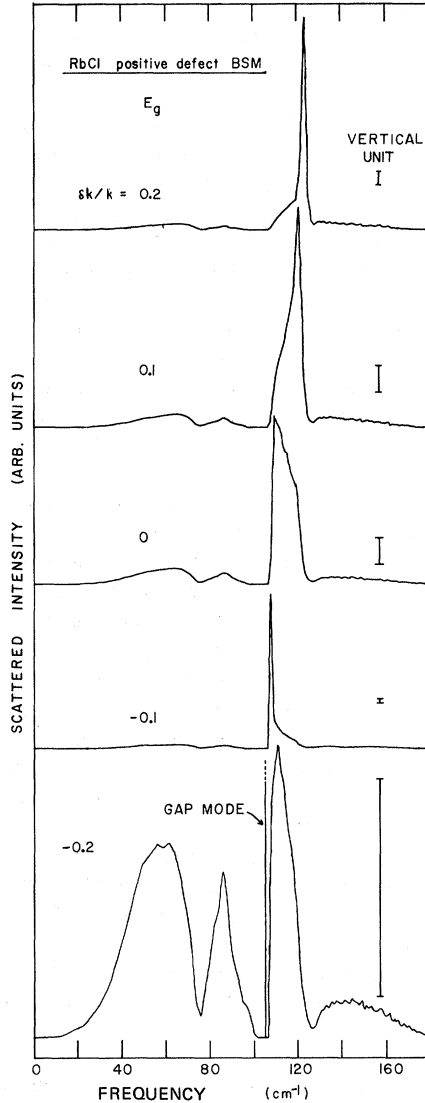FIG. 12. Same as Fig. 8, but for KCl using 115 °K SM (VI) phonons.

FIG. 13. Same as Fig. 8, but for RbCl using 0 °K BSM phonons. The large vertical bar in the lower spectrum reflects the change of the near resonance at 108 cm^{-1} for $\delta k/k = -0.1$ to the localized mode in the gap at 105 cm^{-1} for $\delta k/k = -0.2$.

If it is assumed that the Raman effect is caused by the modulation of the Tl$^+$ electronic wave functions by the vibrations of the nearest-neighbor anions, one can understand qualitatively why the strongest spectral lines in KI and KBr are in the acoustic region of the phonon spectrum, since the anions in these hosts are the heavy ions. In RbCl, where the neighbors are the light ions, the strongest lines lie in the optical-phonon region, while in KCl the spectrum is about equally strong over the entire spectral region, as expected. The strongest lines were always seen to be of E_g symmetry, with weaker lines of T_{2g} symmetry also observed. No significant A_{1g}

spectra were seen.

(ii) Theoretical calculations of the Raman spectra were made using phonons derived from SM and the BSM. In making the calculations it was assumed that the electron-phonon interaction was linear in the displacements of just the defect's nearest neighbors. The best agreement between theory and experiment was obtained by using no force-constant change for the E_g spectra in KI and KBr and for the T_{2g} spectra in all hosts. In KCl, a 10% force-constant stiffening gave the best agreement for E_g, while in RbCl, a 10% weakening gave the best E_g agreement.

(iii) In KBr and KCl, the spectra were calculated using both models for the phonons, and the calculated spectra were essentially similar. This important result means that the eigenvector sums over the Brillouin zone gave virtually identical results for each model. This gives one confidence when using the BSM on hosts for which neutron data and an accompanying SM fit are unavailable.

APPENDIX A: INCLUSION OF PERTURBED PHONONS

For the case of perturbed phonons, the usual Lifshitz techniques may be used to express the perturbed Green's functions in terms of unperturbed ones. Thus, if the harmonic perturbing matrix is defined by

$$\underline{C}(z) \equiv (\underline{\Phi} - \underline{\Phi}_0) - z(\underline{M} - \underline{M}_0) \ ,$$

one obtains from Eq. (15) the result

$$\underline{G}(z) = [\underline{I} + \underline{G}_0(z)\,\underline{C}(z)]^{-1}\underline{G}_0(z) \ . \tag{A1}$$

By expanding the inverse, it is seen that this expression also holds within the harmonic impurity subspace, defined by sites involved with nonzero elements of $\underline{C}(z)$. We consider only longitudinal and transverse force-constant changes $\delta k_l = k_l - k_{l0}$ and $\delta k_t = k_t - k_{t0}$ between the defect and each of its six nearest neighbors. Therefore, our impurity subspace is the same as the subspace defined earlier by the assumed extent of the changed electron-phonon interaction. It is simple to show that

$$\underline{C}(z)\,\underline{\xi}\,(\Gamma_i t) = \delta k_l\,\underline{\xi}\,(\Gamma_i t)$$

for A_{1g} and E_g modes while

$$\underline{C}(z)\,\underline{\xi}\,(T_{2g}t) = \delta k_t\,\underline{\xi}\,(T_{2g}t) \ .$$

Hence, when Eq. (A1) is expressed in the symmetry bases one has

$$g_B\,(A_{1g}) = [1 + \delta k_l g_{B0}\,(A_{1g})]^{-1} g_{B0}\,(A_{1g}) \ , \qquad \text{(A2a)}$$

$$g_B\,(E_g) = [1 + \delta k_l g_{B0}\,(E_g)]^{-1} g_{B0}\,(E_g) \ , \qquad \text{(A2b)}$$

$$g_B\,(T_{2g}) = [1 + \delta k_t g_{B0}\,(T_{2g})]^{-1} g_{B0}\,(T_{2g}) \ , \qquad \text{(A2c)}$$

with the $g_{B0}\,(\Gamma_i)$'s being given as in Eqs. (20), but in terms of unperturbed quantities. For instance, we have

$$\text{Im}g_{B0}\,(A_{1g};\ \omega^2)$$

$$= \pi N^{-1} \sum_{\mathbf{k}j} \delta\,[\omega^2\,(\vec{k}j) - \omega^2]\{|\,e\,(b_2x\,|\,\vec{k}j)|^{\,2}$$

$$\times (1 - e^{i\vec{k}\cdot\underline{R}(-1,1)}) + 4e\,(b_2x\,|\,\vec{k}j)\,e*\,(b_2y\,|\,\vec{k}j)\,e^{i\vec{k}\cdot\underline{R}(2,1)}\} \ .$$

$$\text{(A3)}$$

The real parts of the unperturbed Green's function are Hilbert transforms of the imaginary parts

$$\text{Re}g_{B0}\,(\Gamma_i;\,\omega^2) = \pi^{-1}P \int_0^{\omega_m^2} dx\,[\text{Im}g_{B0}\,(\Gamma_i;x)]\,(x - \omega^2)^{-1},$$

$$\text{(A4)}$$

where ω_m is the maximum frequency in the unperturbed crystal. Knowledge of the real and imaginary parts of the unperturbed Green's functions then enables one to compute the imaginary parts of the perturbed Green's functions. Thus, $\text{Im}g_B\,(T_{2g})$ is given by

$$\text{Im}g_B\,(T_{2g};\omega^2)$$

$$= \frac{\text{Im}g_{B0}(T_{2g};\omega^2)}{[1 + \delta k_t\,\text{Re}g_{B0}\,(T_{2g};\omega^2)]^2 + [\delta k_t\,\text{Im}g_{B0}\,(T_{2g};\omega^2)]^2} \ .$$

$$\text{(A5)}$$

Resonances occur when $1 + \delta k_t\,\text{Re}g_{B0}\,(T_{2g};\omega^2)$ vanishes for ω within the range of unperturbed phonon frequencies, whereas the vanishing of this quantity for frequencies outside the unperturbed range corresponds with the appearance of a localized mode. Whether or not a particular resonance gives rise to a maximum in Eq. (A5) depends, of course, upon the behavior of the imaginary part $\text{Im}g_{B0}\,(T_{2g};\omega^2)$ near the resonance frequency.

Notice that the absolute, rather than the fractional, change of force constant is involved in (A5). Since in alkali halides the magnitudes of the unperturbed longitudinal and transverse overlap force constants are typically in the ratio of 10:1, whereas the Green's functions $g_{B0}(\Gamma_i)$ are of the same order of magnitude for any Γ_i, it is seen that the A_{1g} and E_g phonons are much more strongly perturbed by a given fractional change in k_l than are the T_{2g} modes perturbed by the same fractional change in k_t. Because the changes in k_l and k_t are each derived from the same physical origin, namely, nearest-neighbor overlap, the assumption of approximately equal fractional changes is reasonable and we have accordingly considered the T_{2g} modes to be unperturbed in the numerical calculations presented here.

Considerations similar to those for k_l also hold for possible overlap force-constant changes between the defect and its second or third nearest neighbors. Changes in these quantities are expected to be small in view of the fact that the unperturbed values of these force constants are, if not zero, typically down from those for nearest neighbors by at least an order of magnitude. Furthermore, the possibility of significant relaxation-induced force-constant perturbations between the first and fourth nearest neighbors of the defect, which are nearest neighbors along $\langle 100\rangle$, seems to be excluded by the fact that the ionic radius of Tl$^+$ is but 5% larger than that of K$^+$ and 5% smaller than that of Rb$^+$, the radii being[41] 1.33, 1.40, and 1.48 Å for K$^+$, Tl$^+$, and Rb$^+$, respectively.

Calculated perturbed E_g spectra for a range of weak force-constant perturbations are given in Appendix B.

APPENDIX B: CALCULATED PERTURBED E_g SPECTRA

Here we show in Figs. 8–13 the theoretical perturbed E_g spectra from which the calculations of Figs. 1–3 and Fig. 5 are taken. Greater force-constant changes than ±20% are not shown since they significantly worsen the agreement with experiment.

---

*Work supported by the U. S. Army Research Office, Durham, and by the Advanced Research Projects Agency through the Northwestern University Materials Research Center.

[1]R. T. Harley, J. B. Page, Jr. and C. T. Walker, Phys. Rev. Letters **23**, 922 (1969).

[2]See, for example, in *Light Scattering Spectra of Solids*, edited by G. B. Wright (Springer-Verlag, New York, 1969), pp. 439–562.

[3]J. M. Worlock and S. P. S. Porto, Phys. Rev. Letters **15**, 697 (1965).

[4]D. A. Kleinman, Phys. Rev. **134**, 423 (1964).

[5]G. Benedek and G. F. Nardelli, Phys. Rev. **154**, 872

(1967).

[6]C. H. Henry and C. P. Slichter, in *Physics of Color Centers*, edited by W. B. Fowler (Academic, New York, 1968), p. 351.

[7]C. J. Buchenauer, D. B. Fitchen, and J. B. Page, Jr., in *Light Scattering Spectra of Solids*, edited by G. B. Wright (Springer-Verlag, New York, 1969), p. 521.

[8]B. Fritz, in *Localized Excitations in Solids*, edited by R. F. Wallis (Plenum, New York, 1968), p. 496.

[9]D. W. Feldman, M. Ashkin, and J. H. Parker, Jr., Phys. Rev. Letters **17**, 1209 (1966).

[10]J. A. Harrington, R. T. Harley, and C. T. Walker, Solid State Commun. **8**, 407 (1970).

[11]A. I. Stekhanov and M. B. Eliashberg, Fiz. Tverd. Tela **5**, 2985 (1963) [Soviet Phys. Solid State **5**, 2185 (1964)]; **6**, 3397 (1964) [**6**, 2718 (1965)]; A. I. Stekhanov and T. I. Maksimova, *ibid.* **8**, 924 (1966) [*ibid.* **8**, 737 (1966)].

[12]K. Rebane and I. Tehver, J. Phys. (Paris) **26**, 717 (1965).

[13]R. Kaiser and P. Möckel, Phys. Letters **25A**, 749 (1967).

[14]R. Kaiser and W. Möller, Phys. Letters **28A**, 619 (1969).

[15]R. F. Caldwell and M. V. Klein, Phys. Rev. **158**, 851 (1967).

[16]J. P. Hurrell, S. P. S. Porto T. C. Damen, and S. Mascarenhas, Phys. Letters **26A** 194 (1968).

[17]R. T. Harley, J. B. Page, Jr. and C. T. Walker, Bull. Am. Phys. Soc. **15**, 42 (1970); J. B. Page, Jr., R. T. Harley, and C. T. Walker, *ibid.* **15**, 42 (1970).

[18]L. C. Kravitz, Phys. Rev. Letters **24**, 884 (1970).

[19]Nguyen Xuan Xinh, A. A. Maradudin, and R. A. Coldwell-Horsfall, J. Phys. (Paris) **26**, 717 (1965).

[20]L. Couture and J. P. Mathieu, Ann. Phys. (Paris) **3**, 521 (1948).

[21]G. Dolling, R. A. Cowley, C. Schittenhelm, and I. M. Thorson, Phys. Rev. **147**, 577 (1966).

[22]R. A. Cowley, W. Cochran, B. N. Brockhouse, and A. D. B. Woods, Phys. Rev. **131**, 1030 (1963).

[23]G. Raunio and S. Rolandson, J. Phys. C **3**, 1013 (1970).

[24]J. R. D. Copley, R. W. Macpherson, and T. Timusk, Phys. Rev. **182**, 965 (1969).

[25]G. Raunio and L. Almqvist, Phys. Status Solidi **33**, 209 (1969).

[26]A. A. Maradudin, in *Solid State Physics*, edited by F. Seitz and D. Turnbull (Academic, New York, 1966), Vol. XIX, p. 1.

[27]M. Born and K. Huang, *Dynamical Theory of Crystal Lattices* (Oxford U. P., Oxford, England 1954).

[28]Quantities such as these are often referred to as projected densities of states since, as can be seen from Eq. (15), they consist of the phonon densities of states wieghted by the squared vibrational amplitudes on a subset of particles for modes of a particular symmetry. In the present case the subset consists of the defect's six nearest neighbors.

[29]U. Schröder, Solid State Commun. **4**, 347 (1966).

[30]J. B. Page, Jr. and D. Strauch, Phys. Status Solidi **24**, 469 (1967).

[31]J. T. Lewis, A. Lehoczky, and C. V. Briscoe, Phys. Rev. **161**, 877 (1967).

[32]R. P. Lowndes and D. H. Martin, Proc. Roy. Soc. (London) **A308**, 473 (1969).

[33]J. R. Tessman, A. H. Kahn, and W. Shockley, Phys. Rev. **92**, 890 (1953).

[34]A complete SM theory of Raman scattering would involve the shell as well as the core coordinates explicitly, both in the electron-phonon and perturbed phonon parts of the problem. A consistent SM treatment of perturbed phonons has been given in Ref. 30, and we leave as a problem for further study the application of these ideas to impurity-induced Raman scattering. Thus, we will remain within the present "formal" theory for which the polarization vectors are simply those of the ions or, in the language of the SM, the cores.

[35]In addition to ω^2 being the naturally occurring frequency variable in the theory, its use in numerical work results in the bins having increasing width with decreasing frequency when plotted against ω. This has the effect of putting more points into the acoustic bins than would be the case were the histograms performed for bins of width, say $\Delta\omega = \frac{1}{100}\omega_m$, and hence substantially reduces the low-frequency theoretical uncertainties due to "coarse graining" effects associated with the low-density of phonon frequencies at small ω. Of course the price one pays for this is a loss of resolution due to the use of wider bins at low frequencies, but this should be compensated by the expected lack of strong frequency dependences in this region. The calculated curves are, in fact, quite smooth in the low-frequency acoustic region, with most of the theoretical "noise" occurring in the optical spectra where the bin widths are smallest.

[36]Since Tl^+ is an isoelectronic defect in alkali halides, the Coulomb force constants are, if no relaxation occurs, unperturbed. Hence, our fractional force-constant changes are taken with respect to the unperturbed nearest-neighbor overlap (shell-shell) longitudinal force constant $\frac{1}{2}A$ of the BSM and SM. That is, $\delta k/k$ in our figures is $\delta k_l / \frac{1}{2}A$. The values of A in units of $e^2/(2r_0^3)$ for KI, KBr, KCl, and RbCl are 13.87, 13.07, 12.82, and 13.97 for the BSM, while in the SM for KBr and KCl the values of A are 13.15 and 12.12.

[37]The theoretical doublet in the 157-cm^{-1} peak is not resolved in the experimental data and may be partially due to the narrowness of the bins (1.5 cm^{-1}) at this frequency in the theoretical histograms. The reality of the theoretical doublet could be ascertained by redoing the calculations including more points in the Brillouin zone, either directly or through interpolation schemes. However, this question does not seem sufficiently important to warrant investigation at this time.

[38]D. Bimberg, W. Dultz, K. Fussgänger, and W. Gebhardt, Z. Physik **224**, 364 (1969).

[39]W. B. Fowler, in *Physics of Color Centers*, edited by W. B. Fowler (Academic, New York, 1968), p. 53.

[40]K. Fussgänger, Phys. Status Solidi **34**, 157 (1969); **36**, 645 (1969).

[41]C. Kittel, *Introduction to Solid State Physics*, 3rd ed. (Wiley, New York, 1966), p. 104.